PCCP

PAPER

Check for updates

Second harmonic generation in Janus MoSSe a monolayer and stacked bulk with vertical asymmetry†

Yadong Wei, [ID] [a] Xiaodong Xu, [ID] [a] Songsong Wang, [a] Weiqi Li* [a] and Yongyuan Jiang* [abcd]

A recently synchronized Janus TMD material with broken out-of-plane symmetry offers a vertical dipole to enhance nonlinear optical behavior. Here, by comparing the second harmonic generation properties of MoS_2 and MoSSe monolayers, we investigated the nonzero out-of-plane SHG susceptibilities of a Janus MoSSe 2D material. A three-fold enhancement of out-of-plane SHG susceptibilities exists in three stacked bulks of Janus MoSSe compared to that in the monolayer. A sensitivity to their stack pattern is also found. The broken out-of-plane symmetry, vertical dipole, and intrinsic tunable electronic properties of Janus two-dimensional materials make MoSSe a promising nanomaterial for nonlinear optical devices.

1 Introduction

2D materials provide an ideal platform for fundamental studies and applications in ultrathin nonlinear optical (NLO) devices.[1–3] They exhibit a larger nonlinear optical response than three-dimensional bulk materials,[4–6] which is a primary consideration in developing all-optical communication systems.[7–10] Among the large family of 2D materials, transition metal dichalcogenides (TMDs) have been receiving intensive attention for nonlinear optical applications, because of their highly tunable semi-conducting bandgap and tightly bound electron–hole pairs (excitons).[11–15] One additional compelling aspect of TMDs is the lack of in-plane inversion symmetry of the atomic lattice, allowing for the existence of even-order nonlinear optical processes,[16] such as the electro-optical Pockels effect, optical rectification and second harmonic generation (SHG).[17,18]

Nowadays, the integration of atomic scale ultrathin devices requires advances in exploring the second-order nonlinear optical properties of TMDs in the vertical direction. Unfortunately, the NLO frequency conversion efficiency is still limited by layer numbers. For a hexagonal MoS_2 structure with odd numbers of layers (including the monolayer), its D_{3h} symmetry indicates that it has only four equivalent non-zero second order non-linear susceptibilities.[19] The even number layer and the bulk structures of MoS_2 do not exhibit a second order nonlinear response because the lattice is inversion symmetric. In 2017, Qian[20] studied the multiferroics of the monolayer group IV monochalcogenides MX (M = Ge, Sn, X = S, Se). These 2D materials have a C_{2v} space group, with an inversion symmetry in the vertical direction removed in comparison to the MoS_2 monolayer. As a result, six further different nonzero second order nonlinear susceptibility components one order higher in magnitude than that in MoS_2 monolayer were found.

To break the inversion symmetry in the vertical direction, some approaches were proposed, such as applying static electric fields[21] and biaxial strain,[22] utilizing different crystal phases of the same material[23–25] and changing the composition of atoms in the lattice.

In 2017, Lu[26] and Zhang[27] independently reported the crystal configuration and the synthetic strategy for Janus TMD mono-layers; the stability of the monolayer structure was proved using a phonon dispersion. By replacing one S layer of MoS_2 with Se atoms, the vertical symmetry is broken and a series of intriguing properties was found. For instance, the vertical piezoelectricity[28] d_{33} in multilayer MXY structures is slightly smaller, but still comparable to the 3D piezoelectric material. The broken symmetry and the existence of the electric polarity of a Janus MoSSe monolayer[29] facilitate the Rashba-type spin splitting. In addition, the intrinsic dipole leads to separation of photo-generated electrons and holes,[30] which is crucial in solar water-splitting.

[a] *Department of Physics, Harbin Institute of Technology, Harbin, China.
E-mail: tccliweiqi@hit.edu.cn*
[b] *Collaborative Innovation Center of Extreme Optics, Shanxi University, Taiyuan, China*
[c] *Key Lab of Micro-Optics and Photonic Technology of Heilongjiang Province, Harbin, China*
[d] *Key Laboratory of Micro-Nano Optoelectronic Information System, Ministry of Industry and Information Technology, Harbin, China*
† Electronic supplementary information (ESI) available. See DOI: 10.1039/c9cp03395e
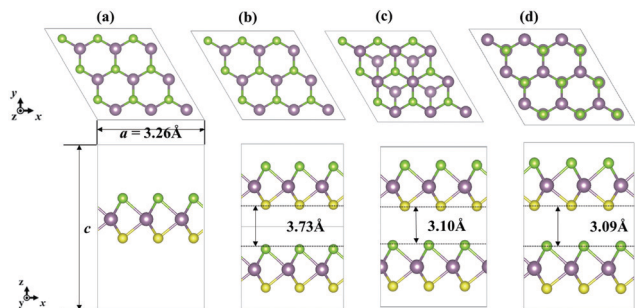
Fig. 1 Illustration of the crystal structures as top and side views. (a) Monolayer MoSSe, (b) AA-stacked bulk MoSSe, (c) AB-stacked bulk MoSSe, and (d) AC-stacked bulk MoSSe. The interlayer distances are indicated.

There are various isomers of Janus TMDs. For the monolayer structures, there is the 1T′ phase whose band structure is quasi-metallic and the 2H phase with a bandgap in the visible light region.[31] For the multilayer structures, the most common, stable and noncentrosymmetric stacked patterns are AA, AB and AC, with the lattice illustrated in Fig. 1. Their stability, and structural and electronic properties have been studied[32–34] systematically. But, the effect of the stacking on the nonlinear optical properties has not been studied yet. For layered materials, Huang *et al.*[35] studied the nonlinear optical properties of two-dimensional GaX (X = S, Se, Te) nanosheets, and they found that the magnitude of SHG coefficients of few-layer bulk GaSe is either independent of or sensitive to the number of layers, depending on the stacked patterns. Moreover, the considerable out-of-plane piezoelectricity was estimated. As a result, it is necessary to study the layer dependence of Janus TMD materials with broken out-of-plane symmetry.

Density functional theory (DFT) based calculation has successfully explained the origin of second harmonic generation (SHG) of some 2D materials. In 2014, Grüning *et al.*[16] found that a SHG signal of MoS_2 monolayer doubles including the electron–hole interaction with respect to the independent electronic transition at a resonance wavelength by a real-time theoretical approach.[36] Guo[37] calculated SHG susceptibilities of MoS_2 monolayer from independent particle approximation (IPA) employing the method reported by Aversa and Sipe.[38] Their results agree well at resonant wavelengths with Grüning's work, although some differences in magnitude appear because of different DFT configurations at large photon energies. Based on the sum-of-state theory described by Sharma *et al.*,[39] Lan[40] successfully divided the nonlinear optical susceptibilities of a semiconductor into two-photon/one-photon transition related terms, and pure interband/intraband related terms, based on the transition matrix generated by DFT wavefunctions.

In this paper, we perform the calculation of SHG properties of Janus MoSSe based on first principles calculations. In Section 2, the method to calculate SHG susceptibilities of both monolayer and stacked bulk Janus MoSSe is presented. The results of SHG calculations are shown in Section 3, including analysis of the electronic band and linear optical response in the monolayer, and stacked nonlinear optical properties in bulk MoSSe structures.

Angular dependence is also analyzed in this part. Finally we conclude this work in Section 4.

2 Model and methods

By substituting one S atom in MoS_2 by Se and forming different stacking patterns, we built four structures, including a mono-layer and AA-, AB-, and AC-stacked pattern structures of Janus MoSSe. The top and side views are shown in Fig. 1. The crystal symmetry is reduced from D_{3h} of MoS_2 to C_{3v}, keeping a three-fold rotational axis along the c direction, as shown in Fig. 1(b)–(d). The space group of the monolayer, and AA and AB stacked bulks is 156, while the AC stacked bulk structure belongs to the space group C_{6v}, with a six-fold screw axis located at the center of the hexagon. Their geometries and ground states were determined from density-functional theory (DFT) calculations using the CASTEP software packages,[41] where the generalized gradient approximation (GGA) parameterized by Perdew and Burke to the exchange–correlation density functional is employed. The energy cut-off is taken as 450 eV, and the Monkhorst–Pack grids are $9 \times 9 \times 1$ and $9 \times 9 \times 9$ for monolayer and bulk, respectively. The convergence criterion is taken as follows: the force on each atom is lower than 0.01 eV Å^{-1} for the geometry optimization. The difference of the total energy is not larger than 10^{-5} eV for the ground state calculations. For the mono-layer calculations, the lattice constant of the supercell along the out-of-plane direction is set as 17.5 Å. For MoSSe stacked bulks, van der Waals interaction is employed between layers by using DFT-D2 modulations of wave functions developed by Grimme.[42] In all calculations, the spin orbit coupling is included. The optimized lattice constant of the MoSSe monolayer is 3.27 Å, which is between that of MoS_2 (3.16 Å) and that of $MoSe_2$ (3.28 Å). The bond lengths of Mo–S and Mo–Se are 2.43 Å and 2.53 Å, respectively. For the bulk MoSSe, interlayer distances are 3.73 Å, 3.09 Å, and 3.10 Å for AA, AB, and AC stacks, respectively. These parameters are indicated in Fig. 1.

The linear optical properties are characterized by the imaginary part of the dielectric function of the four systems using Yambo,[43] a package for excited state calculations in the GW approximation and BSE equation.[36] The Monkhorst–Pack grids are made denser to $24 \times 24 \times 1$ to get the converged dielectric function. The local field effect is considered with random phase approximation, with the screened interaction block size at 30 Ry, the response block size at 5 Ry, and 50 polarization function bands from −15 eV to 15 eV. We did the G_0W_0 calculation with the plasmon-pole approximation with a screened band range from 1 to 70 (from −15 eV to 17 eV). To prevent the convergence problem in many-body calculations, the Random Integration Method is considered in the monolayer case in the first 100 G-components, with 106 random Q points.[44] The truncated Coulomb potential to avoid interlayer interaction is cut off at 32.0 Å along the nonperiodic z direction. Five valence bands and four conduction bands are considered in BSE calculations.

Considering the longer computation time, the second harmonic generation is calculated in the independent particle

This journal is © the Owner Societies 2019

Phys. Chem. Chem. Phys., 2019, **21**, 21022–21029 | **21023**

approximation, introducing a scissor correction based on the linear optical calculations to get the corrected band gap. The real-time approach for the valence states under the external field is implemented to calculate the nonlinear optical response of the system.[36] It is based on the motion equation of the valence state derived by the real-time effective Schrödinger equation

$$i\hbar\frac{d}{dt}|v_{k,m}\rangle = \left(H_k^0 + \Delta H_k\right)|v_{k,m}\rangle + \mathscr{E}|\partial_k v_{k,m}\rangle \qquad (1)$$

where $|v_{k,m}\rangle$ is the time-dependent valence state at the k point and m is the valence band index. H_k^0 is the unperturbed Kohn–Sham Hamiltonian. ΔH_k is the scissor operator discussed above. The local field effects and the time-dependent Hartree approximation can be introduced as the terms following these Hamiltonians. The final term corresponds to the couplings between electric states and external electric field $\mathscr{E}$. According to the modern theory of polarization,[45] the time-dependent polarization is expressed as being proportional to the product of overlap matrix $\langle k,n|k + q,m\rangle$, where $q = b/N_k$, and b is the primitive reciprocal lattice vector of the system. The second harmonic susceptibilities are finally extracted with the power of an electric field. More details are discussed in Attaccalite's work.[36] In this particular case, the grid is taken as $15 \times 15 \times 8$ for the out-of-plane susceptibility components. The G vector participating in the dynamic equation is 2500. The damping factor for the grids is 0.2 eV. Because of the extended vacuum layer thickness of the lattice, we multiply the calculated values by the ratio of parameter c to the thickness of atomic layers. The ratio value is 6 for the monolayer case.

3 Result and discussion

Before calculating the electronic and optical properties, the stabilities of the three stacked patterns need to be determined. We calculated the binding energies by following the expression

$$E_b = E_{stack} - \left(2 \times E_{monolayer}\right) \qquad (2)$$

with E_{stack} being the energy of the stacked pattern lattice, and $E_{monolayer}$ being the energy of the Janus MoSSe single layer. The binding energies of the three stacks are -1.619 eV for AA, -1.800 eV for AB and -1.797 eV for AC, respectively. The phonon dispersion of stacked patterns along the high symmetry path are shown in Fig. S1 (ESI†). There are no soft phonon modes with a frequency less than zero at the Γ point. Moreover, the AB stack pattern, which possesses the lowest binding energy, is the most stable configuration. This agrees well with the previous calculations.[32,46]

3.1 Band structures

Fig. 2(a) The calculated DFT band structure of the MoSSe monolayer, where the bands of the MoS$_2$ monolayer and MoSe$_2$ are also shown for reference. The Fermi level is set to zero for comparing the bandgap. The conduction band minimum (CBM) and the valence band maximum (VBM) for both monolayers are located at the K high-symmetry points, with direct
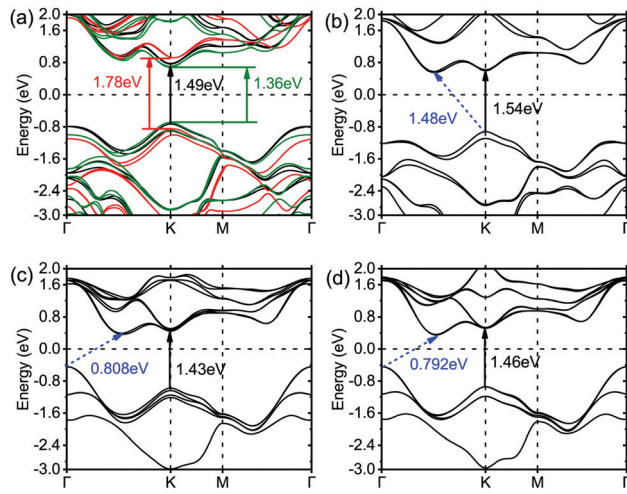

Fig. 2 Band structures of different Janus MoSSe structures: (a) monolayer, and (b) AA-, (c) AB-, and (d) AC-stacked bulks. The spin orbit coupling is included. The red curves in (a) represent the band structure of monolayer MoS$_2$, and the green band structure belongs to monolayer MoSe$_2$. Blue/black arrows refer to the positions of indirect/direct gaps.

bandgaps of 1.78 eV, 1.49 eV, and 1.36 eV, respectively. When spin–orbit coupling (SOC) is considered, the valence band edge shows a nearly 165 meV energy splitting at the K high-symmetry points for monolayer MoSSe, with 150 meV for monolayer MoS$_2$ and 190 meV for monolayer MoSe$_2$; while the splitting at the Γ point is negligible ($\sim$1 meV). These splittings agree with the previous theoretical results.[37] The slightly larger splitting of MoSSe monolayer is induced by the heavier mass of Se atoms. In all MoSSe bulks, the interlayer coupling changes the band structures drastically, similar to the case of MoS$_2$.[38] Their band structures are shown in Fig. 2(b)–(d) with Fermi levels of 7.72, 9.06 and 9.01 eV for AA, AB and AC, respectively. All MoSSe bulks exhibit indirect bandgaps, with valence band edges shifted from the Dirac points to the Γ points. The indirect bandgaps have energies of 1.48, 0.808, and 0.792 eV for AA, AB, and AC stacked bulks, respectively; while the direct bandgaps are still at the Dirac points with energies of 1.54, 1.43, and 1.46 eV, respectively. In the bulks, the valence band SOC splitting energies at the Dirac points are about 60 meV for AA stacked and nearly vanished for the other two types of bulks. They are smaller than that of the monolayer, because of the competition between van der Waals interlayer interactions and SOC effects.[47] The projected band structures of all MoSSe monolayer and bulk cases are plotted in Fig. S2 (ESI†). It is not surprising that there are a few bands among these structures at the VBM and CBM near the K point, which are contributed mainly by the d orbital of Mo atom in all layers. At the Gamma point, the highest energy level is composed of a p orbital of S atom and Mo atom in all systems.

3.2 Linear optical responses

For a weakly applied electric field in the long wavelength limit, the induced electric polarization vector $\mathbf{P}(t)$ can be expanded in

21024 | Phys. Chem. Chem. Phys., 2019, 21, 21022–21029

This journal is © the Owner Societies 2019

terms of the power of the uniform field $\mathbf{E}(t)$ as

$$P_a(t) = P_{0,a} + \int\frac{d\omega}{2\pi}\chi_{ab}^{(1)}(\omega)E_b(\omega)e^{-i\omega t}$$
$$+ \int\frac{d\omega_1 d\omega_2}{(2\pi)^2}\chi_{abc}^{(2)}(\omega_1,\omega_2)E_b(\omega_1)E_c(\omega_2)e^{-i(\omega_1+\omega_2)t} \quad (3)$$
$$+ \dots$$

Here, the subscripts a, b, and c refer to the Cartesian directions x, y, and z, and $E_a(\omega) = \int dt E_a(t)e^{i\omega t}$. The first term $P_{0,a}$ on the right hand side is a static polarization, the second term gives the linear response with the linear susceptibility $\chi_{ab}^{(1)}(\omega)$, and the third term gives the second order response with the second order susceptibility $\chi_{abc}^{(2)}(\omega_1,\omega_2)$. In the following, we present the results for linear susceptibility and second harmonic generation, leaving the zero-order static polarization out of the discussion.

All structures that we investigated either have a C_{3V} or C_{6V} crystal symmetry, from which the components for linear susceptibility are $\chi_{xx}^{(1)} = \chi_{yy}^{(1)} \neq \chi_{zz}^{(1)}$. The dielectric function is given by $\varepsilon_{aa} = 1 + \chi_{aa}^{(1)}$.

Fig. 3 gives the calculated spectra of $Im[\varepsilon_{xx}(\omega)]$ and $Im[\varepsilon_{zz}]$ for monolayer and bulk Janus MoSSe. Several clear features can be seen in the absorption spectrum for the monolayer MoSSe: first, the spectrum under the independent particle approximation with a scissor operator reproduces the features of those using the GW-BSE methods, except a moderate reduction of some absorption peaks, which indicates the excitonic effects. Second, the excitonic effect is more obvious in the monolayer system due to the reduced dielectric screening in atomically thin semiconductors. Third, the values of $Im[\varepsilon_{xx}]$ and $Im[\varepsilon_{yy}]$ in MoSSe monolayer are much larger than that of $Im[\varepsilon_{zz}]$. From Fig. 3(a), it is clear that the first and the second peaks of monolayer MoSSe locate at the photon energies of 1.92 and 2.10 eV. They are induced by the transitions from the two

highest spin-split valence bands to the lowest spin-degenerate conduction band. They correspond to the A and B peak in the MoS$_2$ case, but with a larger splitting energy (~ 30 meV) due to the strong spin–orbit coupling. Those results are in good agreement with Yang's work.[19]

For all bulk MoSSe, the in-plane dielectric tensor components preserve the main features of the MoSSe monolayer. However, the transverse one is obviously enhanced compared to that of MoSSe monolayer due to the induced delocalization by interlayer coupling. Their maximum absorption is located near 2.50 eV with a similar strength to the A and B peaks of the corresponding $Im[\varepsilon_{xx}]$. This indicates that the transverse components of dielectric response are also important in Janus 2D materials, which make them more photophysically characteristic.

3.3 Nonlinear optical susceptibilities

Considering the crystal symmetry C_{3V} of the monolayer and AA and AB stacked bulks, there are in total eleven independent nonzero components for the second order response coefficients: $\chi_{xxz}^{(2)} = \chi_{yyz}^{(2)}$, $\chi_{xzx}^{(2)} = \chi_{yzy}^{(2)}$, $\chi_{zxx}^{(2)} = \chi_{zyy}^{(2)}$, $\chi_{zzz}^{(2)}$, and $-\chi_{yyy}^{(2)} = \chi_{yxx}^{(2)} = \chi_{xyx}^{(2)} = \chi_{xxy}^{(2)}$. Due to the equal incident frequencies in SHG, a further relation can be found as $\chi_{xxz}^{(2)} = \chi_{xzx}^{(2)}$. Compared to MoX$_2$, three additional nonzero components are induced by the reduction of the crystal symmetries, all associated with the z-direction. For the AC-stacked bulk, $\chi_{yyy}^{(2)}$ is zero due to the extra symmetry in C_{6V}. We list all these nonzero components in Table 1.

3.3.1 Monolayers. The SHG spectra of monolayer MoSSe are compared with those of monolayer MoS$_2$ and MoSe$_2$ in Fig. 4(a). The calculated coefficients of MoS$_2$ are similar to those of Grüning's work[32] and Guo's work[26] (0.5 eV to 1.0 eV), either in the position of the first three peaks or the spectral shape below the absorption edge region.

The first peaks locate at nearly 1.0 eV for all monolayer cases. They originate from two-photon excitation at the K high-symmetry point. No significant spin–orbit deviation appears, in contrast to the linear absorption cases. This is attributed to the merge because the spectral distance of A and B peaks is lower than 0.1 eV. The second peaks can be mapped onto the two photon transition from a point between Γ and K, as mentioned in Grüning's work.[32] The third peaks of all monolayers include contributions of both the two photon transition at higher energies larger than 4 eV and one electron excitation at the optical gap. In monolayer MoSSe, this includes a one-photon transition at the K point from its valence band maximum (-0.762 eV) to the conduction band minimum (0.775 eV) and two photon transitions at the Γ point from -1.95 eV to 1.99 eV, respectively. At higher photon energies, the source of peaks is more complex, involving more band transitions.
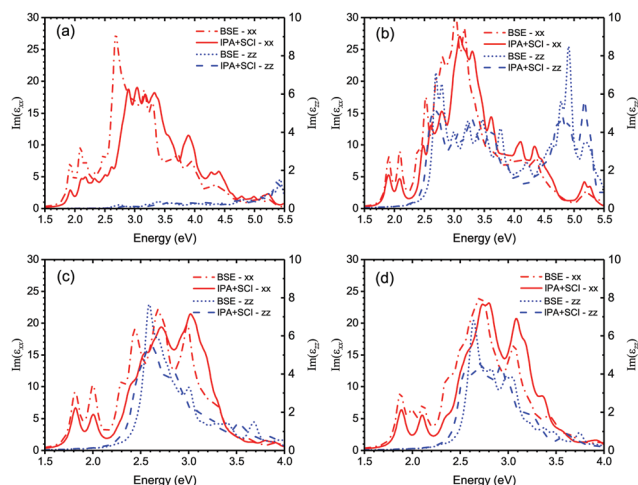

Fig. 3 The imaginary part of the dielectric function ε_{xx}(red) and ε_{zz}(blue) of the (a) 2D monolayer and (b) AA, (c) AB and (d) AC systems; the imaginary part of the dielectric function is calculated at different levels including IPA + SCI and BSE.

Table 1 Nonzero components of conventional and Janus TMD structures

Components	yyy	yzy	zyy	zzz
MoS$_2$	✓			
ML/AA/AB stacked MoSSe	✓	✓	✓	✓
AC stacked MoSSe		✓	✓	✓

This journal is © the Owner Societies 2019

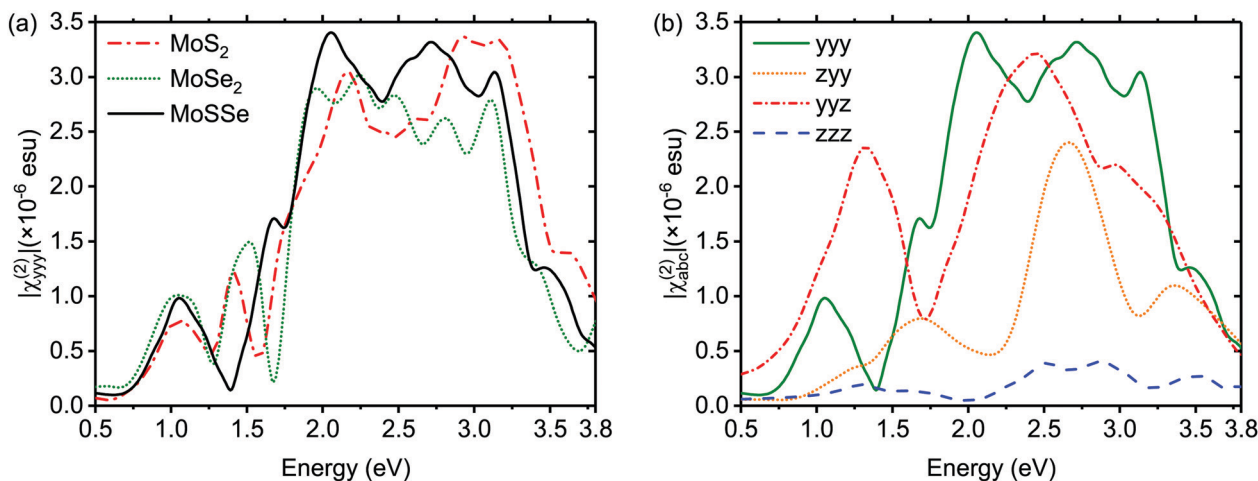*Phys. Chem. Chem. Phys.*, 2019, **21**, 21022–21029 | **21025**

Fig. 4 (a) Absolute values of $\chi_{yyy}^{(2)}$ of monolayer MoSSe (black solid line), MoS$_2$ (red dotted line) and MoSe$_2$ (green dotted line); (b) absolute values of nonzero $\chi_{abc}^{(2)}$ susceptibilities of monolayer MoSSe.

The biggest difference between MoSSe and MoS$_2$ is that the MoSSe monolayer possesses transverse components. In Fig. 4(b), the magnitude of SHG susceptibility $\chi_{zyy}^{(2)}$ is around 2.80×10^{-7} esu, almost one third of that of $\chi_{yyy}^{(2)}$ at 1080 nm pump at the present theoretical level, which is a deviation from the experimental result[26] $|\chi_{yxx}^{(2)}| : |\chi_{zxx}^{(2)}| = 10 : 1$. This magnitude ratio divergence between the measurement and theoretical calculation has been discussed for a long time and is caused by many factors.[36]

However, it is intriguing that these out-of-plane susceptibility components are within an order of magnitude of $\chi_{yyy}^{(2)}$. For instance, the absolute values of $\chi_{zyy}^{(2)}$ are close to those of $\chi_{yyy}^{(2)}$ of MoS$_2$ monolayer at 1064 nm, a common laser wavelength. These components involve the contribution of the z-direction related optical transition. For example, the peak of $\chi_{zyy}^{(2)}$ and $\chi_{zzz}^{(2)}$ at around 2.75 eV corresponds to the peak of 5.50 eV in the linear optical transition (Fig. 3).

3.3.2 Stacked bulk MoSSe structures. The absolute values of $\chi_{yyy}^{(2)}$ components of MoSSe bulks and the monolayer are shown in Fig. 5(a). The $\chi_{yyy}^{(2)}$s of AA and AB stack patterns are both within an order of magnitude of that of the monolayer, while the $\chi_{yyy}^{(2)}$ component of the AC stacked bulk vanishes due to its C_{6v} symmetry. The first peaks of the $\chi_{yyy}^{(2)}$ component of AA, AB and the monolayer cases locate close to each other between 1.00 and 1.50 eV. This peak arises from a direct optical transition at the K high symmetry point, and can be ascribed to a two-photon process. There is only one shoulder at 1.73 eV in the AA and AB stacked bulks, where a second peak is expected as well in the monolayer case. The photon energy matches the two photon transition at the K point, from the energy level -1.40 eV to 1.62 eV. It is close to the third peak, which is generated from the one-photon transition at the K point. As a result, the shoulder other than the independent peak occurs. Without a new peak being generated for these bulk cases, it is implied that the interlayer transitions do not have a large effect on the in-plane components of the SHG response.

Different from bulk MoS$_2$, these stack patterns also possess out-of-plane nonzero SHG coefficients, as shown in Fig. 5(b) and (c).

The $\chi_{zzz}^{(2)}$ component grows stronger in Fig. 5(d), especially in the AB and AC stacks, being nearly eight times larger than that of the monolayer structure at the first peak, where the two-photon process happens. The deviations in SHG response in the bulk cases from the monolayer case are interpreted by the electron transfer between adjacent layers and an interlayer dipole enhancement effect. For AB bulk, SHG susceptibility $\chi_{zyy}^{(2)}$ is nearly twice that of the monolayer and AA bulk. In addition, a three-fold enhancement of the $\chi_{zzz}^{(2)}$ component is also found. Interlayer coupling and dipole–dipole interaction contribute to the strong vertical nonlinear optical response components, being nearly three-fold larger than that in the AA stacked bulk. The absorption edges of the first SHG susceptibility peaks located nearly at half the band gap indicate a two-photon transition process at the optical gap.

3.3.3 SHG polarization response. Measuring the SHG polarization dependence is a noninvasive method to detect the structural anisotropy of a lattice on the microscopic scale.[48,49] In this part, we calculated the SHG polarizations for the Janus MoSSe monolayer and bulk structures. Consider an incident light with an angle θ to the normal line of the monolayer plane and ϕ to the zigzag direction of the TMD monolayer in a plane. Due to the C_{3v} symmetry of Janus MoSSe, two polarization components of the SHG response can be obtained by the following expressions:

$$
\begin{aligned}
I_s &\propto \left(1/2\chi_{yyy}\cos 3\phi\right)^2 I_0^2 \\
I_p &\propto \left(1/2\chi_{yyy}\cos\theta\sin 3\phi - 1/2\chi_{zyy}\sin\theta\right)^2 I_0^2
\end{aligned}
\tag{4}
$$

For the Janus MoSSe monolayer, values of $\chi_{yyy}^{(2)}$ and $\chi_{zyy}^{(2)}$ are 7.95×10^{-7} esu (3.81×10^2 pm V^{-1}) and 2.85×10^{-6} esu (0.967×10^2 pm V^{-1}), respectively, at 1064 nm (1.16 eV) at the IPA theoretical level. It is revealed that SHG polarization depends not only on the polarization angle ϕ, but also on the incident angle θ, where the component $\chi_{zyy}^{(2)}$ is shown. The calculated SHG polarization of the monolayer, and AA and AB
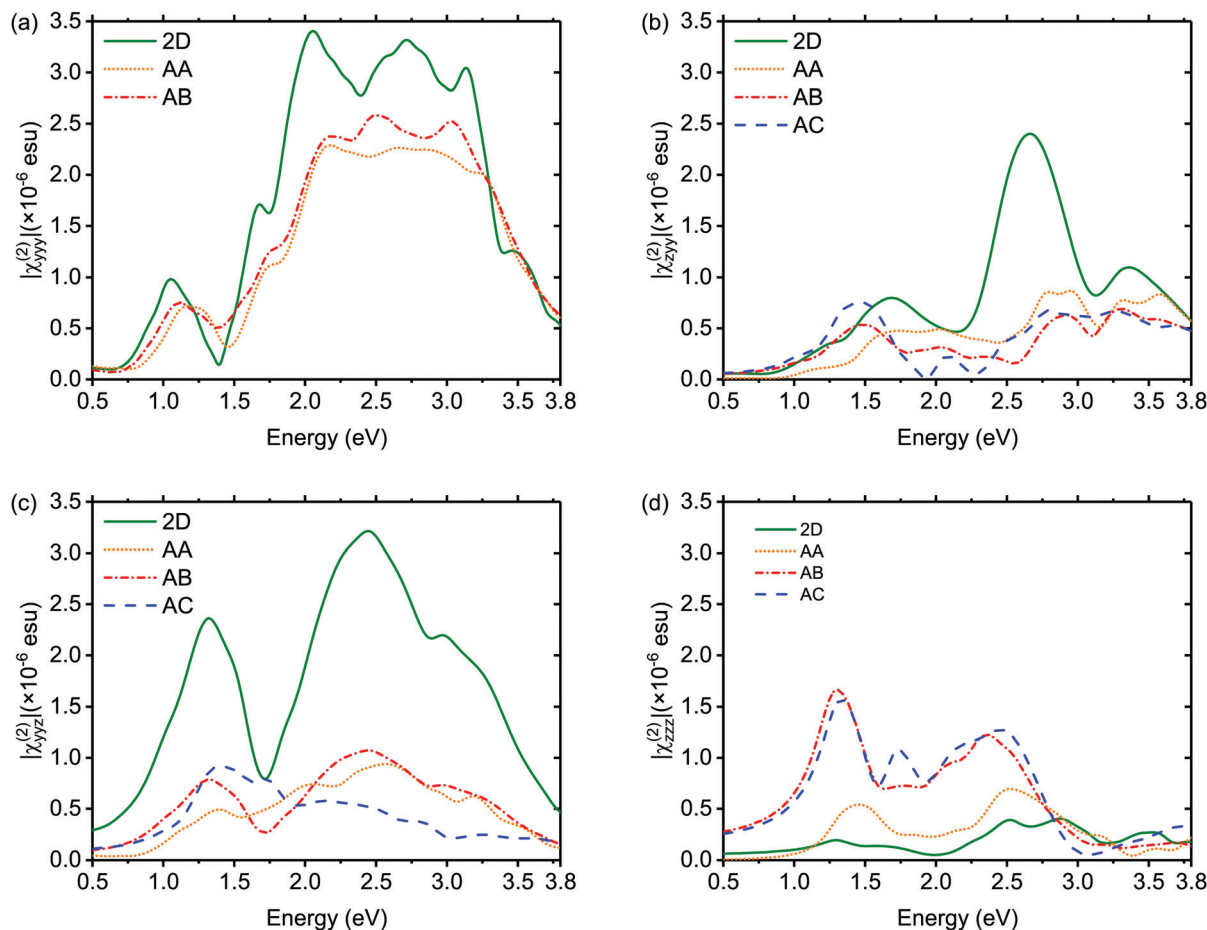
21026 | *Phys. Chem. Chem. Phys.*, 2019, **21**, 21022–21029

This journal is © the Owner Societies 2019

Fig. 5 Absolute values of (a) $\chi^{(2)}_{yyy}$ (b) $\chi^{(2)}_{zyy}$ (c) $\chi^{(2)}_{yyz}$ and (d) $\chi^{(2)}_{zzz}$ in the monolayer (in green solid line) and all stacked bulks (AA in dotted yellow line; AB in red dashed dotted line and AC in blue dashed line) of Janus MoSSe.
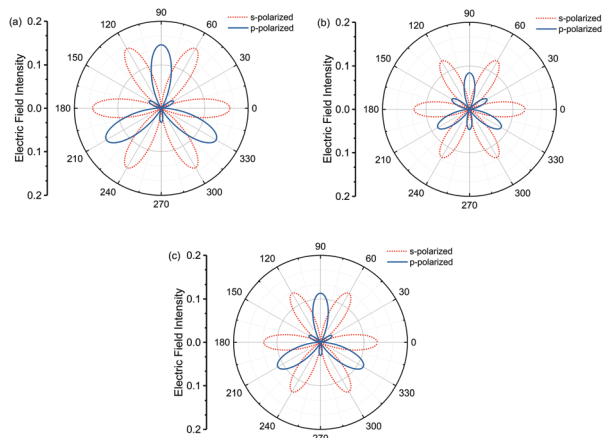

Fig. 6 The s and p polarization of the SHG response of (a) MoSSe monolayer with respect to s polarized incident light, and (b) AA and (c) AB stack with respect to s polarized incident light; the wavelengths of all cases are 1064 nm (1.16 eV). The incident angle is 45°, see text.

stacked bulk of Janus MoSSe is listed in Fig. 6, with the incident angle of 45°. As expected from the C_{3V} symmetry of the monolayer and AB stacked bulk, in addition to the normal six-fold diagram of the polarization direction parallel to the

zigzag direction, we found almost five times stronger and three-fold polarity with light in the armchair direction. When the light was induced perpendicularly to the plane, both s and p polarized responses are six-fold. The polarization diagram for the three structures shown from Fig. S3–S5 (ESI†) indicates that the three-fold polarity appears and grows when the incident angle grows. This is one marked difference from the MoS_2 monolayer polarization map.[48] The relative intensity of SHG response is reduced from the monolayer to AA and AB stacked bulk.

4 Conclusions

In the present work, we reported the second harmonic generation susceptibilities of monolayer and stacked bulks of Janus MoSSe by using first-principles calculations. The results indicate that Janus MoSSe inherits the advantages of known two-dimensional materials. MoSSe monolayer exhibits similar SHG in-plane components to MoS_2 being one order higher than that of lithium niobate.[48] More importantly, broken out-of-plane symmetry in Janus MoSSe increases the number of nonzero independent NLO components, leading to the increase of utilization efficiency of incident light in various directions.

This journal is © the Owner Societies 2019

Phys. Chem. Chem. Phys., 2019, **21**, 21022–21029 | **21027**

Furthermore, the bulk MoSSe shows a nonzero SHG response with an even number of layers. This is different from the vanishing even-order nonlinear optical behavior of conventional TMD bulks. In the end, we calculated the SHG polarization dependence of the Janus MoSSe structures. The symmetry of the polarization changes from six-fold to three-fold with the increase of the incident angle in all monolayer and bulk cases because of the out-of-plane SHG components.

All materials in the present work are transparent below 1.60 eV, which covers the emission lines of most of the currently used lasers. They also exhibit an evident SHG response in this wavelength region that originates from the double-photon and intraband transitions. With large and diverse NLO responses and good chip-integrated ability, Janus 2D layered materials will pave the way for a wide variety of novel applications in NLO fields.

Conflicts of interest

There are no conflicts to declare.

Acknowledgements

Notes and references

1 R. J. Shiue, D. K. Efetov, G. Grosso, C. Peng, K. C. Fong and D. Englund, *Nanophotonics*, 2017, **6**, 1329–1342.

2 B. J. M. Hausmann, B. Shields, Q. M. Quan, P. Maletinsky, M. McCutcheon, J. T. Choy, T. M. Babinec, A. Kubanek, A. Yacoby, M. D. Lukin and M. Loncar, *Nano Lett.*, 2012, **12**, 1578–1582.

3 D. C. Marinica, A. K. Kazansky, P. Nordlander, J. Aizpurua and A. G. Borisov, *Nano Lett.*, 2012, **12**, 1333–1339.

4 K. S. Novoselov, A. K. Geim, S. V. Morozov, D. Jiang, Y. Zhang, S. V. Dubonos, I. V. Grigorieva and A. A. Firsov, *Science*, 2004, **306**, 666–669.

5 X. Jiang, S. Liu, W. Liang, S. Luo, Z. He, Y. Ge, H. Wang, R. Cao, F. Zhang and Q. Wen, *et al.*, *Laser Photonics Rev.*, 2018, **12**, 1700229.

6 A. Autere, H. Jussila, Y. Y. Dai, Y. D. Wang, H. Lipsanen and Z. P. Sun, *Adv. Mater.*, 2018, **30**, 1705963.

7 R. I. Woodward and E. J. R. Kelleher, *Appl. Sci.*, 2015, **5**, 1440–1456.

8 P. D. Dragic, M. Cavillon and J. Ballato, *Appl. Phys. Rev.*, 2018, **5**, 37.

9 Z. P. Sun, A. Martinez and F. Wang, *Nat. Photonics*, 2016, **10**, 227–238.

10 L. M. Wu, W. C. Huang, Y. Z. Wang, J. L. Zhao, D. T. Ma, Y. J. Xiang, J. Q. Li, J. S. Ponraj, S. C. Dhanabalan and H. Zhang, *Adv. Funct. Mater.*, 2019, **29**, 1806346.

11 H. S. Lee, S. W. Min, Y. G. Chang, M. K. Park, T. Nam, H. Kim, J. H. Kim, S. Ryu and S. Im, *Nano Lett.*, 2012, **12**, 3695–3700.

12 D. Mao, B. B. Du, D. X. Yang, S. L. Zhang, Y. D. Wang, W. D. Zhang, X. Y. She, H. C. Cheng, H. B. Zeng and J. L. Zhao, *Small*, 2016, **12**, 1489–1497.

13 D. W. Li, W. Xiong, L. J. Jiang, Z. Y. Xiao, H. R. Golgir, M. M. Wang, X. Huang, Y. S. Zhou, Z. Lin, J. F. Song, S. Ducharme, L. Jiang, J. F. Silvain and Y. F. Lu, *ACS Nano*, 2016, **10**, 3766–3775.

14 N. Kumar, S. Najmaei, Q. Cui, F. Ceballos, P. M. Ajayan, J. Lou and H. Zhao, *Phys. Rev. B: Condens. Matter Mater. Phys.*, 2013, **87**, 161403.

15 D. Xiao, G.-B. Liu, W. Feng, X. Xu and W. Yao, *Phys. Rev. Lett.*, 2012, **108**, 196802.

16 M. Grüning and C. Attaccalite, *Phys. Rev. B: Condens. Matter Mater. Phys.*, 2014, **89**, 081102.

17 R. A. Norwood, C. T. Derose, C. Greenlee and A. Yeniay, *Handbook of Organic Materials for Optical and (Opto)electronic Devices*, Woodhead Publishing, 2010, pp. 709–785.

18 F. Nastos and J. E. Sipe, *Phys. Rev. B: Condens. Matter Mater. Phys.*, 2006, **74**, 035201.

19 R. W. Boyd, *Nonlinear Optics*, Academic Press, Inc., 3rd edn, 2008, p. 640.

20 H. Wang and X. F. Qian, *Nano Lett.*, 2017, **17**, 5027–5034.

21 H. K. Yu, D. Talukdar, W. G. Xu, J. B. Khurgin and Q. H. Xiong, *Nano Lett.*, 2015, **15**, 5653–5657.

22 H. Yu, D. Talukdar, W. Xu, J. B. Khurgin and Q. Xiong, *Nano Lett.*, 2015, **15**, 5653–5657.

23 J. Liang, J. Zhang, Z. Li, H. Hong, J. Wang, Z. Zhang, X. Zhou, R. Qiao, J. Xu, P. Gao, Z. Liu, Z. Liu, Z. Sun, S. Meng, K. Liu and D. Yu, *Nano Lett.*, 2017, **17**, 7539–7543.

24 K.-I. Lin, Y.-H. Ho, S.-B. Liu, J.-J. Ciou, B.-T. Huang, C. Chen, H.-C. Chang, C.-L. Tu and C.-H. Chen, *Nano Lett.*, 2018, **18**, 793–797.

25 W.-T. Hsu, Z.-A. Zhao, L.-J. Li, C.-H. Chen, M.-H. Chiu, P.-S. Chang, Y.-C. Chou and W.-H. Chang, *ACS Nano*, 2014, **8**, 2951–2958.

26 A.-Y. Lu, H. Zhu, J. Xiao, C.-P. Chuu, Y. Han, M.-H. Chiu, C.-C. Cheng, C.-W. Yang, K.-H. Wei and Y. Yang, *et al.*, *Nat. Nanotechnol.*, 2017, **12**, 744.

27 J. Zhang, S. Jia, I. Kholmanov, L. Dong, D. Er, W. Chen, H. Guo, Z. Jin, V. B. Shenoy and L. Shi, *et al.*, *ACS Nano*, 2017, **11**, 8192–8198.

28 L. Dong, J. Lou and V. B. Shenoy, *ACS Nano*, 2017, **11**, 8242–8248.

29 T. Hu, F. Jia, G. Zhao, J. Wu, A. Stroppa and W. Ren, *Phys. Rev. B: Condens. Matter Mater. Phys.*, 2018, **97**, 235404.

30 X. C. Ma, X. Wu, H. D. Wang and Y. C. Wang, *J. Mater. Chem. A*, 2018, **6**, 2295–2301.

31 Z. Wang, *J. Mater. Chem. C*, 2018, **6**, 13000–13005.

32 Z. Y. Guan, S. Ni and S. L. Hu, *J. Phys. Chem. C*, 2018, **122**, 6209–6216.

33 Y. Yang, Y. Zhang, H. Ye, Z. Yu, Y. Liu, B. Su and W. Xu, *Superlattices Microstruct.*, 2019, **131**, 8–14.

34 W.-J. Yin, B. Wen, G.-Z. Nie, X.-L. Wei and L.-M. Liu, *J. Mater. Chem. C*, 2018, **6**, 1693–1700.

21028 | *Phys. Chem. Chem. Phys.*, 2019, **21**, 21022–21029

This journal is © the Owner Societies 2019

35 L. Hu, X. Huang and D. Wei, *Phys. Chem. Chem. Phys.*, 2017, **19**, 11131–11141.

36 C. Attaccalite and M. Grüning, *Phys. Rev. B: Condens. Matter Mater. Phys.*, 2013, **88**, 235113.

37 C. Y. Wang and G. Y. Guo, *J. Phys. Chem. C*, 2015, **119**, 13268–13276.

38 C. Aversa and J. E. Sipe, *Phys. Rev. B: Condens. Matter Mater. Phys.*, 1995, **52**, 14636–14645.

39 S. Sharma and C. Ambrosch-Draxl, *Phys. Scr.*, 2004, **T109**, 128–134.

40 Y.-Z. Lan, *Computational Condensed Matter*, 2016, **8**, 22–30.

41 S. J. Clark, M. D. Segall, C. J. Pickard, P. J. Hasnip, M. J. Probert, K. Refson and M. C. Payne, *Z. Kristallogr.*, 2005, **220**, 567–570.

42 S. Grimme, J. Antony, S. Ehrlich and H. Krieg, *J. Chem. Phys.*, 2010, **132**, 154104.

43 A. Marini, C. Hogan, M. Gruening and D. Varsano, *Comput. Phys. Commun.*, 2009, **180**, 1392–1403.

44 O. Pulci, G. Onida, R. Del Sole and L. Reining, *Phys. Rev. Lett.*, 1998, **81**, 5374.

45 R. Resta, *J. Phys.: Condens. Matter*, 2000, **12**, R107.

46 S.-D. Guo, *Phys. Chem. Chem. Phys.*, 2018, **20**, 7236–7242.

47 G. Wang, C. Robert, M. Glazov, F. Cadiz, E. Courtade, T. Amand, D. Lagarde, T. Taniguchi, K. Watanabe and B. Urbaszek, *et al.*, *Phys. Rev. Lett.*, 2017, **119**, 047401.

48 Y. L. Li, Y. Rao, K. F. Mak, Y. M. You, S. Y. Wang, C. R. Dean and T. F. Heinz, *Nano Lett.*, 2013, **13**, 3329–3333.

49 R. Cisek, D. Tokarz, N. Hirmiz, A. Saxena, A. Shik, H. E. Ruda and V. Barzda, *Nanotechnology*, 2014, **25**, 505703.